ACS NANO

www.acsnano.org

Article

Charge Transfer between Quantum Dots and Redox Molecules Is Not Auger-Assisted

Yan B. Vogel,* Willemijn Boeije,# Lotte van Steekelenburg,# Demi Vollebregt, Reinout Ubbink, Hua Chen, Ali Tayefeh Younesi, Ronald Ulbricht, Wolter F. Jager, Ferdinand Grozema, and Arjan J. Houtepen

Cite This: *ACS Nano* 2026, 20, 3487−3498

Read Online

ACCESS | Metrics & More | Article Recommendations | Supporting Information

ABSTRACT: Charge transfer between quantum dots (QDs) and redox molecules is not well described by the Marcus theory, the hall-mark theory for charge transfer in molecular systems. The Marcus inverted region, where the rate decreases with increasing the free energy difference, has never been observed in QDs. The previously reported hypothesis for the absence of the Marcus inverted region in QDs is an Auger-assisted charge transfer pathway, which we refer to as the "Auger hypothesis". Here, we show that the Auger hypothesis does not hold to experimental tests. We measured the rate constants for two processes where Auger is either allowed or not: charge separation and charge recombination. We used ultrafast transient absorption spectroscopy to probe the rate of charge separation and recombination between PbS QDs and ferrocene derivatives ligands bound to their surface. We find that the rate constant for both charge separation and recombination increases by increasing the free energy difference, is temperature-independent, and increases with the number of molecular acceptors. All these results are against theoretical predictions for an Auger-assisted charge transfer pathway.

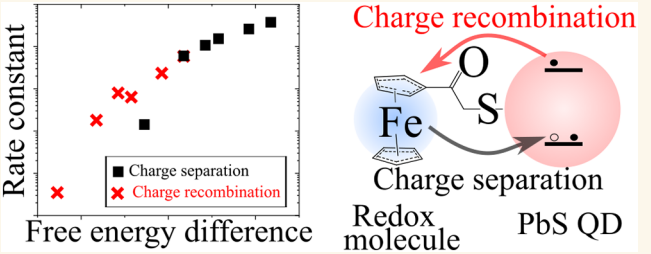

KEYWORDS: *charge transfer, electron transfer, hole transfer, quantum dot, nanocrystal, molecular acceptor, Marcus theory*

MAIN

The field of quantum dot (QD) is making tremendous progress in developing diverse technologies like light-emitting diodes,[1−4] photodetectors,[5−7] lasers,[8−10] photocatalysts,[11,12] and solar energy harvesters.[13,14] All these technologies rely on charge transfer to function, and attaining their full potential requires a deep understanding of the mechanism of charge transfer. For example, a QD photodetector or solar cell requires efficient charge extraction of the photogenerated exciton, commonly performed by hole and electron transport layers. These transport layers are charge acceptors, often molecular acceptors, determining device efficiency. Hence, optimization of charge transfer between the QD and the molecular acceptor is an important factor when building photodetectors and solar cells. This is also true for building light-emitting devices, where charges are injected into QDs through these charge acceptor molecules. In fact, these devices are often engineered based on our knowledge of energy levels alignment between these layers to optimize charge extraction. Besides the technological importance, electron transfer is of special fundamental interest as the simplest chemical reaction, showcasing the difficulty of scientific understanding even for the simplest physicochemical phenomena. All these considerations have led to a rich literature investigating the mechanisms of charge transfer in QDs that has been extensively reviewed.[15,16] Nonetheless, important fundamental questions have not been resolved. In particular, experimental tests on the mechanism of charge transfer between QDs and redox molecules (A) disagree with predictions from the Marcus theory,[17−20] the hall-mark theory for charge transfer in molecular systems.

Here, we consider photoinduced charge transfer in a QD-A complex (QDA, Figure 1A).[21−30] Figure 1B shows a scheme of the steps involved in photoinduced charge transfer for a QDA system. Photoexcitation of the QD leads to the excited complex QD*A (Figure 1B, gray arrow). Subsequently, the charge separated state (QD^-A^+ for hole transfer) forms upon electron transfer from A to QD (Figure 1B, red arrow), referred to as charge separation (CS). Finally, electron transfer from QD back to A (Figure 1B, blue arrow) leads to the initial ground state QDA, referred to as charge recombination (CR). The Marcus theory assumes that the standard free energies

Received: August 14, 2025
Revised: December 24, 2025
Accepted: December 24, 2025
Published: January 15, 2026

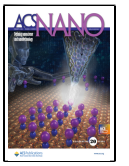

https://doi.org/10.1021/acsnano.5c13838
ACS Nano 2026, 20, 3487−3498

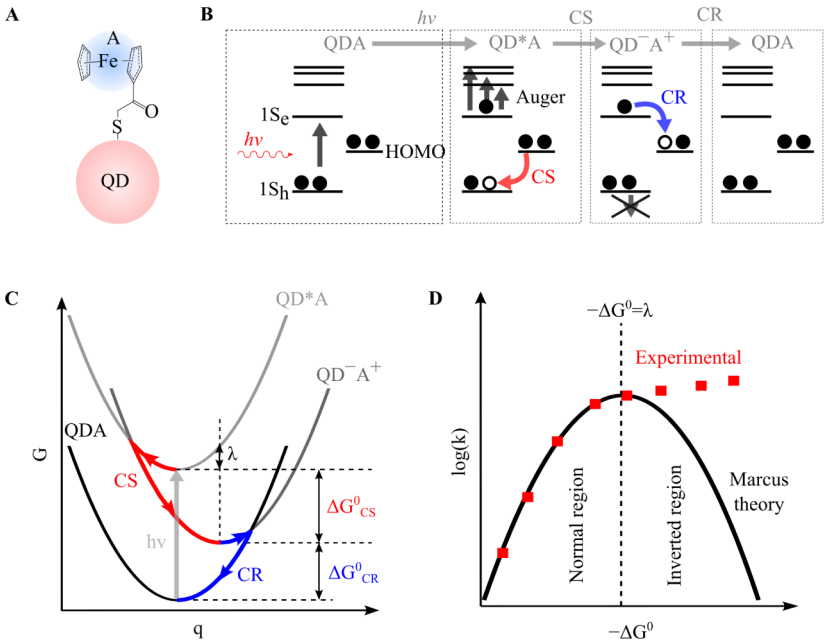

Figure 1. Theoretical description of charge transfer from quantum dots to redox molecules. (A) Scheme of a quantum dot-redox molecule complex (QDA). (B) Schematics of photoinduced charge transfer for QDA: (1) photoexcitation ($h\nu$) of QD to form the excited state (QD*A), (2) charge separation (CS) to form the charge separated state (QD^-A^+) and (3) charge recombination (CR) back to the ground state (QDA). (C) Standard free energy (G) as a function of the reaction coordinate (q) for QDA, QD*A and QD^-A^+. The pathway for CS and CR is shown in red and blue arrowed lines, respectively. The free energy of electron transfer ($\Delta G°$) is given by the difference between the minima in the curves, and the reorganization energy (λ) by the energy necessary to bring the equilibrium state of the reactant to the equilibrium state of the product (or *vice versa*) (D) Rate constant (k) as a function of $\Delta G°$, as predicted by eq 1 (solid line) and the previously experimentally observed trend for QDs (red symbols).[17,18]

(G) of the species involved in charge transfer depend quadratically on the reaction coordinate (q), as schematically shown in Figure 1C. The Marcus theory considers charge transfer to occur without the gain or loss of energy and with all the nuclear positions frozen during the charge transfer event. Hence, charge transfer occurs at the intersection of the two G-q curves, as represented by the red and blue arrows in Figure 1C for CS and CR, respectively. These assumptions lead to an expression for the rate constant of charge transfer (k):[31]

$$k = \frac{2\pi}{\hbar} H_{QDA}^2 (4\pi\lambda k_B T)^{-1/2} \exp\left[-\frac{(\Delta G° + \lambda)^2}{4\lambda k_B T}\right] \quad (1)$$

Where λ is the reorganization energy, the energy necessary to transform the nuclear configurations from reactants to products (at their equilibrium geometry), $\Delta G°$ is the free energy difference between QD^-A^+ and QD*A (for CS) or between QDA and QD^-A^+ (for CR), H_{QDA} is the electronic coupling between QD and A, $\hbar$ is the reduced Planck constant, T the temperature and k_B the Boltzmann constant.

A striking prediction of eq 1 is a decrease in k with increasing $|\Delta G°|$ for $|\Delta G°| > \lambda$, known as the inverted region (Figure 1D). The region for $|\Delta G°| < \lambda$ where k increases with $|\Delta G°|$ is known as the normal region (Figure 1D). This prediction was experimentally confirmed for intramolecular charge transfer in organic molecules,[32,33] leading to the Nobel Prize in Chemistry for Rudolph Marcus in 1992.[34] Subsequent studies have experimentally verified the theoretical $k - \Delta G°$ relationship for various systems, including intramolecular charge transfer in inorganic complexes,[35] proton-coupled electron transfer reactions,[36] and charge transfer between bulk semiconductors and redox molecules.[37−39] In addition, instances of charge transfer in molecular systems not following the Marcus relationship are now well understood in molecular systems. These include diffusion limited intermolecular charge transfer,[40] the formation of electronically excited products after CS,[41] barrierless charge transfer,[42] and electron transfer between metals and redox molecules.[43]

In contrast, charge transfer between quantum dots and redox molecules is much less understood. Several groups recently reported the absence of the inverted region for charge transfer in QDA complexes.[17−19] A flattening of k with increasing $|\Delta G°|$ beyond λ occurs instead (Figure 1D, red symbols). This behavior has been tentatively explained by suggesting the presence of a coupled Auger-like transition in which the excess of free energy is consumed by a transition of the residual photogenerated charge carrier to deeper levels inside the band (Figure 1B).[17,18] We refer to this explanation as the "Auger hypothesis". The Auger hypothesis could explain well most of past kinetic studies because they focused on investigating CS.[17,18] CS could indeed be Auger-assisted because of the presence of free "spectator" charges at the band-edge, in line with the Auger hypothesis. On the other hand, the absence of such additional charges during CR prevents Auger transitions within the QDs (Figure 1B). Although Auger transitions could still happen within the molecular acceptor, this can be avoided by selecting a molecular acceptor where other transitions are too high in energy to occur. Taking these considerations into account, comparison between CS and CR provides a means of testing the "Auger hypothesis", which is the main aim of this article.

It is also worth considering studies in contradiction with the Auger hypothesis. This includes the study of Wang et al. which reported the relationship of the CR rate constant as a function

https://doi.org/10.1021/acsnano.5c13838
ACS Nano 2026, 20, 3487−3498

of $\Delta G°$.[19] This work showed no inverted regime, which would speak against the Auger hypothesis. However, the lack of inverted region was instead rationalized by postulating that the inverted region is masked by an increase in H_{QDA} when decreasing the QD size to change $\Delta G°$. To support their hypothesis, Wang et al. showed that normalization of the rate by H_{QDA} (calculated through an effective mass model) does result in the predicted inverted region. However, this reasoning relies heavily on the correctness of the calculation of H_{QDA}. The work by Chemmangat et al. also points to the absence of Auger, as they did find the Marcus inverted region for CS in perovskite QDs.[44] Nevertheless, a direct test of the Auger hypothesis by comparing both CS and CR rates over a wide $\Delta G°$ range is still missing.

With this study we seek to experimentally test the Auger hypothesis to gain further understanding of the mechanism of charge transfer in QDs. We constructed a model system that allows comparing rate constants of CS and CR over a wide $\Delta G°$ range beyond λ. A direct comparison of both CS and CR in a similar $\Delta G°$ range provides a means to test the Auger hypothesis. If the Auger hypothesis is correct, the CS rate constant would increase monotonically with $\Delta G°$ (Figure 1D, red symbols), while the CR rate constant would depend quadratically on $\Delta G°$ (Figure 1D, solid line), showing an inverted region. We emphasize the importance of being deep inside the inverted region for testing the Auger hypothesis.

In our model system, we use PbS QDs and determine the rate constants of both CS and CR by ultrafast transient absorption spectroscopy measurements. We covalently attach ferrocene hole acceptors onto the PbS QD surface to form the QDA complexes. Ferrocene is a well-suited hole acceptor for testing the Auger hypothesis because the HOMO accepting the hole is far away in energy from other electronic states, preventing any possible electronic transition of the created hole. Ferrocene has a HOMO−LUMO gap of 2.7 eV, preventing any electron transitions to upper levels, and the characteristic blue color of ferrocenium is due to the LMCT at 2.0 eV, which also prevents hole transitions to lower levels. Further, the small bandgap of PbS (0.41 eV for bulk) and the large HOMO−LUMO gap of the ferrocene (2.7 eV) allows to selectively photoexcite the QDs without photoexciting the ferrocene. In addition, PbS QDs exhibit a long radiative lifetime,[45] similar electron and hole effective masses and equal $1S_e$ electron and $1S_h$ hole degeneracies.[46] All this simplifies interpretation of the charge carrier dynamics and allows to observe both CS and CR. The small effective electron/hole mass and large dielectric constant of PbS allow to tune the $1S_e$ and $1S_h$ (i.e., the LUMO and HOMO) levels of the QDs and hence $\Delta G°$ over a wide range.[47] Crucially, the use of tetrachloroethylene as solvent and ferrocene give a small λ. As discussed in Section S1 of the Supporting Information, we estimate a solvent reorganization energy of 20 meV and an inner reorganization energy of 40 meV, giving a total reorganization energy of 60 meV. The small value of λ means that the inverted region is easily accessible, as it occurs when $|\Delta G°| > \lambda$. In our system, we can decrease $\Delta G°$ down to −850 meV, vide infra, which gives us access deep into the inverted region.

Importantly, we control the number of acceptor molecules per QD through ligand exchange and quantify this number from the Fe to Pb atomic ratio measured by X-ray photoelectron spectroscopy. Knowledge of the number of acceptor molecules is required because (i) we need to extract the rate constants, which are normalized by the number of redox molecules, and (ii) the dependence of charge transfer on the number of acceptor molecules has been found experimentally to be not straightforward.[22,24,48−50] We find that the rates of both CS and CR depend linearly on the number of acceptor molecules.

To achieve modulation of $\Delta G°$, we vary the QD size to tune the bandgap energy by approximately 700 meV. This well-controlled system allows to change $\Delta G°$ while minimizing the variation of other parameters that influence k. We find that the rate constants of both CS and CR increase with $\Delta G°$ even beyond λ and therefore does not show the predicted Marcus inverted region. We therefore conclude that Auger recombination cannot be the sole explanation, as CR does not involve Auger.

To gain further insight into the charge transfer mechanism we performed temperature-dependent transient absorption spectroscopy measurements. The temperature-dependent CS and CR rate constants reveal that the process is activationless over the whole range of free energies explored, rather than at one value of $\Delta G°$, as predicted by the Marcus model.

RESULTS AND DISCUSSION

Development of the Experimental Model

We developed an experimental model with careful control of the parameters described in eq 1 and their dependencies. A detailed discussion on the dependencies of these parameters is included in Section S1 and S2 of the Supporting Information. Briefly, we varied $\Delta G°$ by changing the bandgap energy of the PbS QDs through quantum confinement. We controlled the QD to A distance to ensure H_{QDA} and λ are kept constant, and controlled the number of A and excitons (N) per QD to determine the rate constant k from the rate Γ. Importantly, employing transient absorption spectroscopy on PbS QDs with ferrocene ligands, we could measure the relationship between k and $\Delta G°$ described in eq 1 for both CS and CR. In this section we describe the experimental model used and its characterization.

Our experimental model consists of a dispersion in tetrachloroethylene of PbS QDs with covalently anchored ferrocene-ethan-2-one-1-thiol ($FcOC_2SH$ hereinafter) as the molecular hole acceptor. This QDA complex is referred to as PbS-$FcOC_2SH$ hereinafter (Figure 1A). We synthesized PbS QDs by hot-injection of bis(trimethylsilyl) sulfide into a solution of lead-oleate in octadecene, as reported by Hines and Scholes,[51] followed by isolation and redispersion in tetrachloroethylene (see Methods for details). We varied the QD diameter from 2.5 to 5.7 nm by adjusting the synthesis temperature and precursor ratio (Figures S1 and S2). The 1S absorption peak varied from 0.89 to 1.61 eV (Figure 2B, black solid lines, and Figure S3). TEM images (Figure S2) show quasi-spherical PbS QDs with a narrow size distribution. The as-synthesized PbS QDs have a symmetric Gaussian photoluminescence spectrum, indicating the absence of trap-mediated radiative recombination pathways (Figure 2B, red dashed lines). Consistent with previous reports, the PbS feature a decrease in Stokes shift and PL lifetime (see next section) with decreasing bandgap (Figure 2B).[45,52,53]

We used ferrocene as a molecular charge acceptor because it features ideal reversible redox chemistry[54] and versatile organic chemistry.[55] Importantly, the latter allowed the synthesis of $FcOC_2SH$ (see Methods for details), a molecule consisting of a

https://doi.org/10.1021/acsnano.5c13838
ACS Nano 2026, 20, 3487−3498

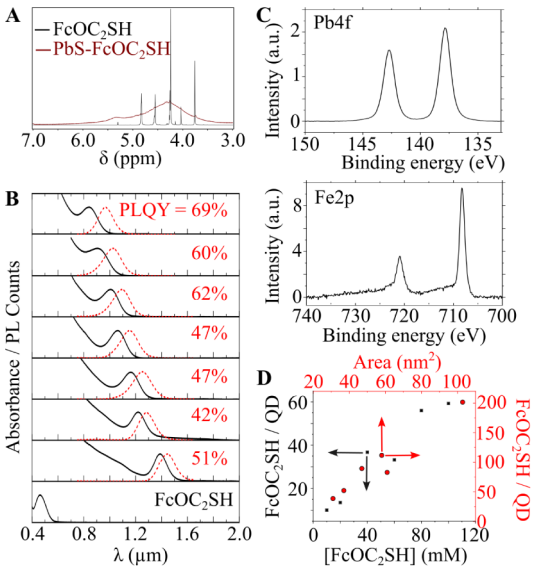

Figure 2. Characterization of the experimental model. (A) ^{1}H NMR of $FcOC_2SH$ (black line) and PbS-$FcOC_2SH$ QDs (red line, d = 3.6 nm) in $CDCl_3$. The inset shows a scheme of the developed QDA system. (B) Absorption (black solid line) and photoluminescence (red dashed line) spectra of PbS QDs. The inset shows the PLQY. (C) Pb 4f (top) and Fe 2p (bottom) X-ray photoelectron spectra of PbS-$FcOC_2SH$ (d = 3.9 nm and [$FcOC_2SH$] = 100 mM). (D) Experimentally determined number of $FcOC_2SH$ per QD as ($FcOC_2SH$/QD) a function of the [$FcOC_2SH$] used during ligand exchange for PbS QDs of 25 nm^2 in area (black squares, d = 2.8 nm), and as a function of the QD surface area for [$FcOC_2SH$] = 50 mM during ligand exchange (red circles).

ferrocene group as the redox molecule with a 2-propanonethiol group as a linker between the ferrocene and the PbS QD (Figure 1A). The thiolate group offers a strong anchoring point to the PbS surface, in contrast to the much weaker binding of carboxylate ligands.[56] This allows fixing the electron transfer distance and controlling the number of redox molecules per QD. This last aspect is important because the rate depends both on the distance and number of acceptors (eq 1, S1 and S7)). We confirmed successful binding between the ferrocene and PbS by ^{1}H NMR spectroscopy, as shown in Figure 2A. The peaks at 4.83, 4.55, and 4.24 ppm in the pure $FcOC_2SH$ spectrum correspond to the H from the cyclopentadiene rings, and the peak at 3.70 ppm corresponds to the H from the alkyl chain (Figure 2A, black line). All the $FcOC_2SH$ peaks broaden after attachment to the PbS QD (Figure 2A, red line). The broad peak at 5.35 ppm for the PbS-$FcOC_2SH$ QDs corresponds to oleate ligands, which is also evident for the as-synthesized PbS QDs (Figure S4). The broadening of the $FcOC_2SH$ peaks between 5.0 and 3.5 ppm after attachment is evidence that the $FcOC_2SH$ becomes attached to a larger object, restricting its rotational mobility and resulting in line broadening (Figure 2A).[57] The absence of sharp peaks confirms the absence of unbound $FcOC_2SH$ in solution.

Since the NMR results show that all $FcOC_2SH$ is bound to the PbS QDs, we quantified the number of $FcOC_2SH$ molecules per quantum dot ($FcOC_2SH$/QD) by determining the Fe to Pb ratio (Fe/Pb) by X-ray photoelectron spectroscopy (Figures 2C, S5–S12 and Table S1). To translate the obtained Fe/Pb to $FcOC_2SH$/QD, we obtained the total number of Pb in a QD with knowledge of the QD volume (obtained by TEM and assuming QDs are perfect spheres) and the PbS density. The results show that $FcOC_2SH$/QD increases with increasing $FcOC_2SH$ concentration used during ligand exchange ([$FcOC_2SH$], black data points in Figure 2D). We also found that $FcOC_2SH$/QD increases with increasing QD surface area (red data point in Figures 2D and S13–S15, the surface area was obtained from the QD diameters determined by TEM and assuming they are perfect spheres). Values ranged from 3 to 200 $FcOC_2SH$/QD. The control of the number of $FcOC_2SH$ molecules per QD is a crucial consideration because determination of the rate constant requires knowledge of this number. In addition, how the rate of charge transfer depends on the acceptor's concentration is not well understood.[24,48−50]

After ligand exchange with $FcOC_2SH$, the $1S_h1S_e$ peak of the PbS QDs absorption spectrum generally broadened and red-shifted (Figure S16). The shift and broadening of the $1S_h1S_e$

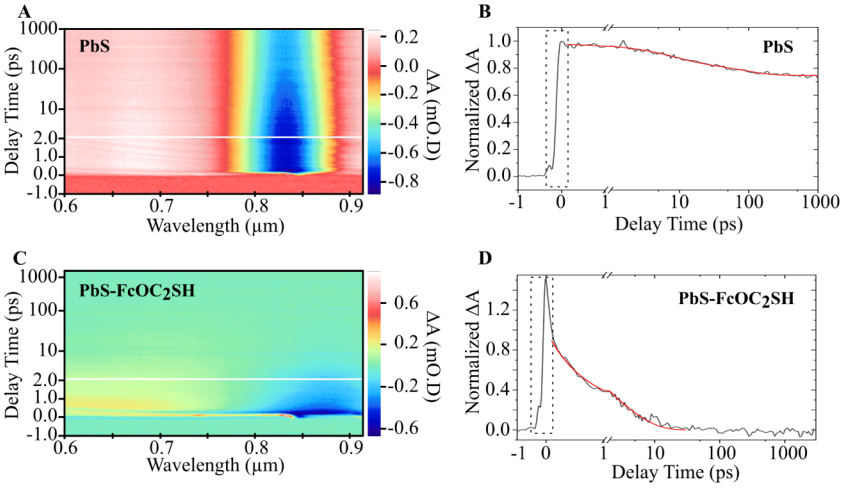

Figure 3. Charge transfer dynamics of PbS (top) and PbS-$FcOC_2SH$ (bottom). Transient absorption hyperspectral images and the respective transients at the $1S_h1S_e$ peak position of (A, B) PbS and (C, D) PbS-$FcOC_2SH$ with a bandgap of 1.48 eV and 2.8 nm in diameter, and with $FcOC_2SH$/QD = 37 for the latter. In (B, D) the black line is the experimental data, the red line is a biexponential fit, and the dashed box highlights the coherent artifact.

https://doi.org/10.1021/acsnano.5c13838
ACS Nano 2026, 20, 3487−3498

peak increased with increasing $FcOC_2SH$/QD (Figure S16). Because we observe the same effect upon anchoring an alkanethiol group (Figure S17), we attribute this effect to electronic coupling between the QDs and the thiol group, slightly increasing the size of the PbS QDs. In addition, we also observed complete PL quenching after $FcOC_2SH$ ligand exchange, but not after ligand exchange with the alkanethiol group, a first indication of efficient charge transfer between PbS and $FcOC_2SH$.

Charge Carrier Dynamics

We next probed the dynamics of the photoexcited charge carriers in PbS and PbS-$FcOC_2SH$ QDs by transient absorption (TA) spectroscopy from ~150 fs to ~3 ns in the near-infrared spectral region. We excited the QDs at the $1S_h1S_e$ band-edge transition to prevent hot carrier generation, which could induce hot carrier charge transfer, complicating the interpretation of the measurements. We excited the QDs in the low fluence limit, in which the average number of excitations per QD <*N*> was lower than 0.1 and the probability of forming biexcitons is <1% (see Section S5 of the Supporting Information for details). We probe changes in the absorption of the PbS QDs in our TA experiments and all transients shown below represent the transient absorption at the $1S_h1S_e$ peak of the PbS QDs. For sake of simplicity, we first focus our discussion on two samples: PbS and PbS-$FcOC_2SH$ QDs with a bandgap of 1.48 eV (i.e., diameter of 2.8 nm), and with $FcOC_2SH$/QD = 37 for the latter. TA data for all samples as a function of QD diameter and $FcOC_2SH$/QD are shown in Figures S18–S24, but the features discussed in this section are general for all samples.

Figure 3A–D shows the TA transients in absence (Figure 3A,B) and presence (Figure 3C,D) of the molecular acceptor. The TA transients show an early time signal in the first ~250 fs that appears over the whole spectrum, which is due to the pump–probe coherent artifact (dashed box in Figure 3B,D),[58] and that we leave out in further analysis. The TA signal for PbS without molecular acceptors is long-lived and only shows a minor decay of ~20% due to charge trapping (Figure 3A,B). We describe this trapping process in detail in Section S7 of the Supporting Information. In contrast, in the presence of the molecular acceptor the signal completely decays to zero within the measurement time scale (Figure 3C,D). It is well established that for Pb-chalcogenide QDs both the electron and the hole give rise to an absorption bleach.[59,60] Hence, the fact that the bleach fully disappears means that both the hole and the electron have disappeared from the $1S_h$ and $1S_e$ levels, respectively, and that both charge separation and recombination take place within the 3 ns time-window of the experiment.

The whole process can be described by a biexponential function of the form (see section S10 of the Supporting Information for a full description of the decay kinetics to arrive at this equation):

$$\frac{\Delta A}{\Delta A_{max}} = \frac{1}{2}e^{-k'_{CS}t} + \frac{1}{2}e^{-k'_{CR}t} \quad (2)$$

The two rate constants k'_{CS} and k'_{CR} here reflect the charge separation and recombination. The biexponential fit (Figure 3D, red line) reveals a lifetime of ~1 ps and ~5 ps. To test whether the increased rates for CS and CR could be due to newly introduced traps, we attached the same ferrocene molecule through a 2-hexanone linker (ferrocene-hexan-6-one-1-thiol, $FcOC_6SH$, synthesis described in the Methods) to the PbS QDs. The longer linker makes the charge transfer lifetime fall in the order of hundreds of nanoseconds, as evidenced by time-resolved photoluminescence spectroscopy (Figure S30). Importantly, no decay is evident within the 3 ns TA time window (Figure S31). The lack of decay means that the attachment of thiol functionalized ferrocene ligands does not introduce surface trap states, other than the ferrocene itself.

Importantly, the rates of CS and CR are nearly 2 orders of magnitude higher than the trapping and trap-recombination rates in absence of $FcOC_2SH$. CS to $FcOC_2SH$ will strongly outcompete any trapping on uncontrolled surface states. Hence, we discard the trapping channels in the analysis of TA transients for the PbS-$FcOC_2SH$ samples, and the data are fitted with eq 2.

Concentration-Dependent Charge Carrier Dynamics

After understanding the charge carrier dynamics, we explored the effect of $FcOC_2SH$/QD on the rates. Figure 4A (solid lines) shows the TA decays at the $1S_h1S_e$ peak of PbS-$FcOC_2SH$ QDs of 3.1 nm in diameter and a bandgap of 1.37 eV for different $FcOC_2SH$/QD (see also Figure S24 for the respective hyperspectral TA images). A biexponential fit to the TA decays (Figure 4A, dashed lines) reveals the pseudo first order rate constants of CS and CR (k'_{CS} and k'_{CR}). Figure 4B shows that both k'_{CS} (black squares) and k'_{CR} (red circles) increase linearly with increasing $FcOC_2SH$/QD. The linear increase of k'_{CS} with the number of $FcOC_2SH$ agrees with the expectation from eq S7. Therefore, we obtain the CS *rate constant*, k_{CS} (k_{CS} = 2.5 x10^{10} s^{-1} mol^{-1}) using eq S7, which is what is needed to evaluate eq 1.

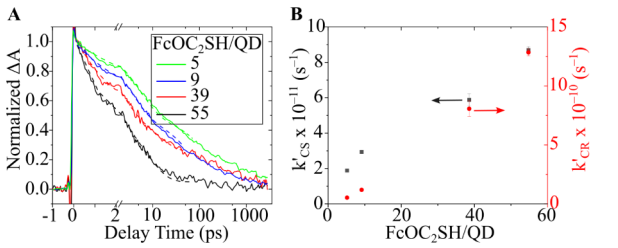

Figure 4. Charge transfer dynamics dependence on the number of acceptors per QD. (A) Time decays of PbS-$FcOC_2SH$ with a bandgap of 1.37 eV and 3.1 nm in diameter for $FcOC_2SH$/QD of 5 (green line), 9 (blue line), 39 (red line) and 55 (black line). The experimental data (solid lines) were fitted to a biexponential function (dashed lines, eq 2). (B) Pseudo first order rate constants for CS (k'_{CS}, black squares, left) and CR (k'_{CR}, red circles, right) as a function of the number of redox molecules per QD, $FcOC_2SH$/QD, as determined from the biexponential fittings shown in (A).

We would expect k'_{CR} to be independent of the number of $FcOC_2SH$ molecules per QD because the electron transfer occurs from the QD to a single oxidized molecule (Fc^+OC_2SH), eq S8. Therefore, the measured k'_{CR} should in principle be equal to the CR rate constant, k_{CR}. However, as shown in Figure 4B, we find that k'_{CR} also increases with $FcOC_2SH$/QD. The dependence of k_{CR} on $FcOC_2SH$/QD indicates that there is a parameter in eq 1 that scales with $FcOC_2SH$/QD. We postulate that this parameter is H_{AD}. The increase of H_{AD} with increasing $FcOC_2SH$/QD could occur if the acceptors coordinate on the surface with different configurations. Then, the probability of an ideal configuration that maximizes H_{AD} would increase with $FcOC_2SH$/QD. In subsequent analysis, we normalize k'_{CR} by the number of

https://doi.org/10.1021/acsnano.5c13838
ACS Nano 2026, 20, 3487–3498

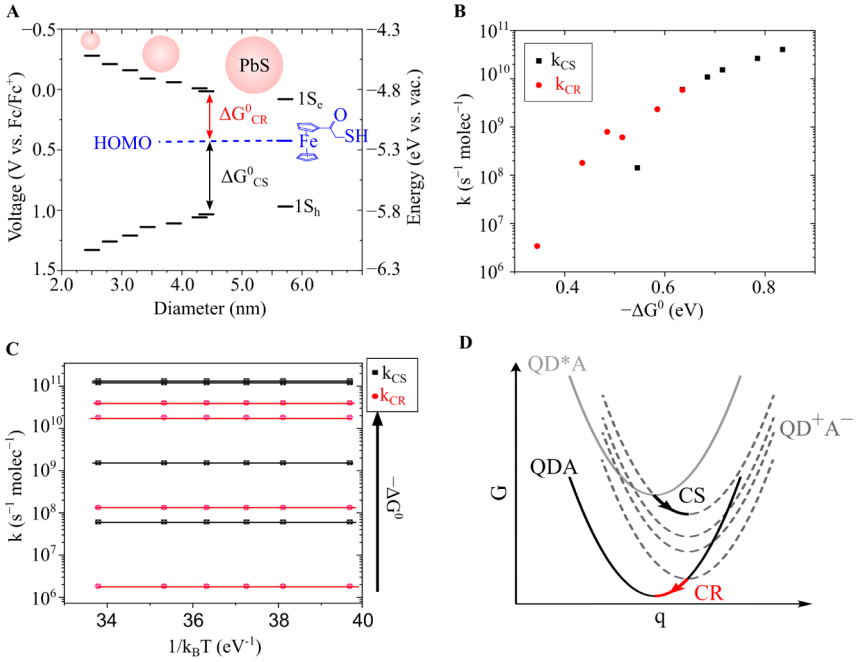

Figure 5. The dependence of charge carrier dynamics on free energy difference and temperature. (A) Scheme showing the absolute energy levels of the QD and $FcOC_2SH$, and the increase in free energy $\Delta G°$ of CS and CR, with decreasing QD diameter (and increasing bandgap). (B) Experimentally measured rate constants for CS (black squares) and CR (red circles) as a function of $-\Delta G°$. (C) Temperature (in)dependence of the rate constant for CS (black squares) and CR (red circles) at increasing $-\Delta G°$ (from 350 mV to 850 mV, bottom to top). (D) Standard free energy (G) as a function of the reaction coordinate (q) for QDA, QD*A and QD^-A^+. The pathway for CS and CR is shown in black and red arrowed lines, respectively. QD^-A^+ shows many displaced energy surfaces representing the different QDA configurations. Charge always transfers across the activationless pathway.

acceptors to consider its scaling with $FcOC_2SH$/QD (k_{CR} = 1.7×10^9 s^{-1} mol^{-1}). In any case, we note that the dependence of k_{CR} on $FcOC_2SH$/QD does not qualitatively affect the discussion that follows, since this dependence is much smaller than that of changing the QD diameter (shown in next section). In addition, the presence of multiple configurations is in line with the temperature-dependent kinetic results discussed below.

The Dependence of Charge Carrier Dynamics on Free Energy

Having developed a reliable method to determine k_{CS} and k_{CR}, we now determine their dependence on $\Delta G°$. To access the Marcus inverted region, it is necessary to have a range in $\Delta G°$ larger than the reorganization energy. We varied $\Delta G°$ by leveraging the E_{BG} tunability of the QDs with their diameter. As the diameter decreased from 5.7 to 2.5 nm, the bandgap increased from 0.89 to 1.61 eV, covering a range of 720 meV (see Figure S3). If we assume that the $1S_e$ and $1S_h$ levels shift symmetrically with bandgap (as theoretically predicted from the similar electron and hole effective mass of PbS),[46] $\Delta G°$ spans over a range 360 meV for both CS and CR. However, experimentally it has been found that the $1S_e$ level varies roughly twice more with size than the $1S_h$ level,[59] which would translate to a $\Delta G°$ range of 240 meV for CS and 480 meV for CR. In any scenario the change in $\Delta G°$ is much larger than the estimated λ of 60 meV making the inverted region easily accessible.

Besides the relative change in $\Delta G°$, to test eq 1 it is convenient to know the absolute magnitude of $\Delta G°$. The value of $\Delta G°$ is given by the energy alignment between the $1S_e$ (or $1S_h$) level and the highest occupied molecular orbital (HOMO) level of $FcOC_2S$, as explained in detail in Section S2 of the Supporting Information. Cyclic voltammetry (Figure S25) showed that the HOMO level of $FcOC_2SH$ is at 0.425 V vs Fc/Fc^+ (−5.225 eV vs vacuum). It has been previously argued that the HOMO level of ferrocene is independent of the surrounding chemical environment because of the charge in the central ferrocene is shielded by the cyclopentadienyl rings (the ferrocene assumption).[61] Therefore, the HOMO level of ferrocene should not be affected by the type of solvent used and the proximity of the QD. On the other hand, the $1S_h$ and $1S_e$ absolute energy levels of QDs are more difficult to determine. We previously reported the $1S_h$ and $1S_e$ absolute energy levels of PbS QDs of various diameters, capped with different ligands, and dispersed in different electrolytes by spectroelectrochemistry.[59] However, we cannot use the energy level values of our previous study because the PbS QDs used here have different ligands and are dispersed in a different solvent. Both the ligands and the solvent can change the QDs $1S_h$ and $1S_e$ levels by several eV.[59,62] The PbS QDs used in this study were dispersed in tetrachloroethylene, a solvent not compatible with these electrochemical measurements.

To circumvent this problem, we estimated the energy level alignment from the kinetic data obtained as a function of E_{BG} (Figure S33). The only assumption we make here is that the reorganization energy and electronic coupling in eq 1 are identical for CS and CR. Under this assumption, the rate constants of CS and CR would be equal for the same free energy difference that (*i.e.*, k_{CS} = k_{CR} for $\Delta G°_{CS}$ = $\Delta G°_{CR}$). Hence, we determined the energy level offset at which the CS and CR rate constants are equal for the same $\Delta G°$ value. A full description of this procedure is included in Section S8 of the Supporting Information. This results in an alignment with the HOMO level shifted 100 meV upward in energy from the

https://doi.org/10.1021/acsnano.5c13838
ACS Nano 2026, 20, 3487−3498

midbandgap, with ΔG° spanning from −350 meV to −850 meV, as shown in Figure 5A.

Figure 5B shows the relationship between k_{CS} (black squares) and k_{CR} (red circles) as a function of ΔG°. We find that the values of both k_{CS} and k_{CR} increase over 4 orders of magnitude within increasing ΔG° from −350 meV to −850 meV. We note that $-\Delta G^\circ$ is several times higher than the estimated λ (60 meV), hence the system is expected to lie deep into the inverted region for all QD sizes. However, a striking observation in Figure 5B is that neither CS nor CR shows a decrease in rate constant predicted by eq 1 for $\Delta G^\circ > \lambda$: there is no evidence for the Marcus inverted region in either CS or CR. This conclusion does not change if we use a different energy alignment.

As discussed in the introduction, the absence of an inverted region for charge transfer from QDs to redox molecules has been reported before.[17−19] This was previously explained by suggesting that Auger recombination with the additional photogenerated carrier (here the electron) introduces additional charge transfer pathways, masking the inverted region of each individual pathway. During the CR process, no additional charge carrier is present for such Auger processes. However, it is clear from Figure 5B that the Marcus inverted region is also absent from the CR process. We thus conclude that Auger recombination cannot be the explanation.

The Temperature Dependence of Charge Carrier Dynamics

To understand what mechanism is responsible for the unexpected absence of the Marcus inverted region in both CS and CR we measured the temperature dependence of these rates, over a T range from 20 to 70 °C. The obtained TA decays are shown in Figure S34 of the Supporting Information and the obtained rates are shown in Figure 5C. Surprisingly we find that temperature has no detectable effect on either CS or CR, for any of the samples studied. Hence, the process is activationless for the whole range of free energy differences explored for both CS and CR. The experimentally observed activationless process contrasts with the Marcus theory, which predicts an activationless process only for the specific case of $\lambda = -\Delta G^\circ$. We note that the rate would vary 115% within this temperature range for an activation energy in the order of thermal energy, which we could easily detect with our experiments. In practice, one would expect activation energies from 0.35 to 2.5 eV for this system, considering the estimated values of $-\Delta G^\circ$ and λ, resulting in rates varying from 3 to 8 orders of magnitude over the studied temperature range.

The temperature dependent measurements rule out several activated mechanisms that could otherwise mask the inverted region. This includes an increase in H_{QDA} with decreasing the QD diameter. This possibility has been considered previously, and the rates were corrected with theoretically calculated values of H_{QDA}.[18,19] Although H_{QDA} could change with QD diameter, the process would remain activated and therefore should show dependence of the rate with temperature. We also rule out a large λ as an explanation of the absence of the inverted region. It has been suggested that λ for nonpolar solvents can be several hundred of meV higher than theoretically predicted.[63−65] However, this situation would involve a large activation barrier, hence a strong temperature dependence. Finally, we also note that an activationless process would be in line with an Auger-assisted model for CS; however, CR cannot be Auger-assisted and therefore is not in line with our experimental results.

We also rule out several activationless mechanisms that could be in line with the temperature-dependent measurements. This includes adiabatic charge transfer that occurs for strong electronic coupling which would be barrierless and largely temperature independent. The rate for adiabatic charge transfer can be estimated using the Fermi Golden Rule. It is proportional to the square of the electronic coupling which is only weakly dependent on temperature.[66] We discard this possibility because the rates for such strong coupling are expected to be higher than 10^{13} s^{-1}, while all our rates are below 10^{11} s^{-1}. We also discard trap assisted charge transfer as an activationless mechanism. Olshansky et al. previously measured the dependence with temperature of the rate constant for CS.[20] They observed a weak temperature dependence that yielded a small activation energy of 60−90 meV, and that remained constant with varying the free energy. They explained this observation considering a trap-mediated charge transfer process. However, we discard this possibility here because the rates of CS and CR are much faster than the trapping rates. In addition, the fraction of QDs with traps ranges from 10% to 30%, which also exclude trap mediated charge transfer as the dominant pathway in CS and CR.

An alternative mechanism that is in line with the experimental results presented above is the existence of multiple QDA configurations. A configuration describes the interaction between the molecule and the QD. The difference in interaction could be due to the molecule anchoring to different positions on the QD surface (different facets, edges), different binding geometries (e.g., sitting straight or lying down), or having a different chemical environment (e.g., different solvation, number of neighboring ligands or redox molecules around it). Therefore, each configuration is described by a different free energy surface, as schematically shown in Figure 5D. Charge transfer is dominated by the configuration with the lowest activation energy. This is in fact the same explanation that we presented above for the observation of the concentration dependence on the rate of CR. According to this "configuration hypothesis" the rates for both CS and CR increase with increasing the number of acceptors (Figure 4B), decreasing free energy (Figure 5B) and be independent of temperature (Figure 5C). This hypothesis explains the common observation of nearly activationless charge transfer commonly observed in QDA systems before.[20,67] It is interesting to consider a limit for the configuration hypothesis for QDs with a single molecular acceptor, where we would expect to observe temperature dependence and the normal and inverted regions. This is also true for systems with homogeneous configurations, which could also explain the recent results by Chemmangat et al.[44] Therefore, further research exploring more rigid linkers, QDs having only a single molecular acceptor, or using single-dot spectroscopy is necessary to confirm the configuration hypothesis.

CONCLUSIONS

We have demonstrated that the absence of the Marcus inverted region in quantum dots is not due to the prevalent hypothesis of an Auger-assisted charge transfer. We have tested this hypothesis by measuring charge transfer of a process that could be Auger-assisted and another that cannot, namely charge separation and recombination, respectively. The results show

https://doi.org/10.1021/acsnano.5c13838
ACS Nano 2026, 20, 3487−3498

the absence of an inverted region for both processes, ruling out an Auger-assisted pathway. Temperature-dependent transient absorption spectroscopy measurements for both charge separation and recombination for a wide range of free energies point that an activationless charge transfer mechanism is always present, regardless of the driving force. The temperature-dependent measurements discard various possible charge transfer pathways previously proposed for not finding the Marcus inverted region in QDs, including the scaling of the electronic coupling with size, and a very large value for the reorganization energy. These results, together with the rate of charge recombination dependence with acceptor concentration, suggest the presence of multiple molecular configurations as the reason behind the absence of the inverted region. The "configuration hypothesis" is in line with other studies showcasing the overlooked importance of the orientation of molecular acceptors at the quantum dot surface. For example, Morris-Cohen et al. found rates insensitive to the linker length, in disagreement with the theoretically expected exponential decrease in rate constant with distance, in line with multiple molecular configurations.[68] In another study, Bird et al. show rates correlate with the way the molecular acceptor binds to the surface.[69] Our work also points to the importance that molecular configurations play in charge transfer. In any case, we emphasize that further research is necessary to test the validity of the configuration hypothesis. Testing this hypothesis could be done by exploring systems with single molecular acceptors together with the use of single-dot spectroscopy.

Our results will inspire future theoretical and experimental studies on the mechanism of charge transfer in quantum dot systems. It provides a clear guideline on the experiments necessary to perform to further test the mechanism of charge transfer between quantum dots and molecular acceptors. This is not a trivial task. First, it requires a fine control and understanding over alternative charge transfer pathways of the specific system being tested, including trapping and coupled electronic transitions in both the QDs and the molecular acceptor. Second, it is necessary to build an experimental system that allows to change the free energy without substantially affecting other parameters such as electronic coupling, acceptor−donor distance and reorganization energy. Third, it requires a strong and irreversible linkage between the molecular acceptor and the QD, with control and access of the number of molecular acceptors per QD. Fourth, it is necessary to use an experimental tool to access charge carrier dynamics over several orders of magnitude for both the charge separation and recombination processes. Fifth, and often disregarded, it is very important to access to the activation energy using temperature-dependent kinetic measurements to understand if the process is thermally activated in the first place. Finally, access to experimental kinetic data at the single nanoparticle level of a QD with a single acceptor could clarify the mechanistic picture of charge transfer in the QD field. Ultimately, this information could lead to new means of controlling the mechanism of charge transfer between quantum dots and redox molecules and the optimization of QD technology.

MATERIALS

All materials were purchased from Sigma-Aldrich unless otherwise stated. For the synthesis of PbS QDs we used lead(II) oxide (PbO, 99.999%), octadecene (ODE, 90%), bis(trimethylsilyl) sulfide (TMS, synthesis grade), and oleic acid (OA, extra pure, Thermo Fisher Scientific). For the synthesis of the ferrocene derivatives, we used 6-bromohexanoyl chloride (97%), chloroacetyl chloride (98%), aluminum chloride ($AlCl_3$, 98%, anhydrous), dichloromethane (DCM, ≥99.8%, anhydrous), ferrocene (Fc, 98%), hexamethyldisilathiane ($(TMS)_2S$, synthesis grade), tetrahydrofuran (THF, 99.9%, anhydrous), and tetra-*n*-butylammonium fluoride (TBAF, 1.0 M solution in THF). For the ferrocene derivatives workup we used magnesium sulfate ($MgSO_4$), and silica gel (siliaflash, 40−63 μm, Silicycle), and technical grade dichloromethane, petroleum ether, and ethyl acetate. All NMR were performed in deuterated chloroform (+0.03% TMS, 99.80%, Eurisotop). The QDs were dispersed in tetrachloroethylene (TCE, ≥99%, anhydrous) for further analysis, except for NMR.

Synthesis of PbS QDs

PbS QDs were synthesized following a previously described procedure.[51] In a typical synthesis, lead(II) oxide (90 mg) was dissolved in OA (0.25 mL) and ODE (3 mL) by heating under vacuum to 100 °C for 1 h. The temperature was then set to the desired temperature (e.g., 150 °C), and a solution of TMS (42 μL) in ODE (0.75 mL) was injected under a nitrogen atmosphere. The heating mantle was lowered away from direct contact with the reaction flask immediately after injection of the TMS solution and allowed to cool to room temperature. The PbS QD size was adjusted by modifying the OA/Pb/S ratio (from 4:2:1 to 80:2:1) and temperature (115−150 °C). The PbS QDs were isolated from the reaction mixture by adding acetone until the solution became turbid, centrifuged, the supernatant removed, and the QDs redispersed in 8 mL of tetrachloroethylene. The QD dispersion was stored at room temperature.

Synthesis of Ferrocene-ethan-2-one-1-thiol ($FcOC_2SH$)

The synthesis of $FcOC_2SH$ consisted in a Friedel-Craft acylation to obtain 2-ferrocene-ethan-2-one-1-chloride ($FcOC_2Cl$) which has been previously described,[70] followed by a thiolation to obtain the final product ($FcOC_2SH$). **Synthesis of $FcOC_2Cl$.** $FcOC_2Cl$ was synthesized following a previously described procedure.[70] Ferrocene (15 g, 81 mmol) and DCM (100 mL) were added to a 250 mL three-neck round-bottom flask under argon and cooled to −15 °C. Chloroacetyl chloride (6 g, 53 mmol) was added to the flask. Anhydrous $AlCl_3$ (7.15 g, 54 mmol) was added slowly over a period of 4 h, keeping it stirring, at −15 °C, and under argon. After addition, the reaction was allowed to reach room temperature and kept stirring overnight. The reaction was quenched with ice and extracted with DCM and water. The organic layer was dried by magnesium sulfate, and the solvent was evaporated by a rotary evaporator. The obtained solid was purified by column chromatography with an eluent of hexane/DCM (2:1), and the solvent was evaporated by a rotary evaporator to obtain $FcOC_2Cl$ (5.5 g, 21 mmol, 40% yield). ^{1}H NMR (399.7 MHz, Chloroform-d): δ = 4.8 (m, 2H), 4.6 (m, 2H), 4.4 (s, 2H), 4.2 (s, 4H). ^{13}C NMR (100 MHz, Chloroform-d): δ = 195.3, 75.9, 73.0, 70.2, 69.5, 46.0 ppm. **Synthesis of $FcOC_2SH$.** A 100 mL round-bottom flask was charged with $FcOC_2Cl$ (2.75 g, 10 mmol), and THF (20 mL) was added under argon. $(TMS)_2S$ (3.16 mL, 15 mmol) was added under stirring and cooled to −15 °C. A TBAF solution (15 mL, 15 mmol, 1 M in THF) was added dropwise to the solution, allowed to reach room temperature, and let react for 1 h at room temperature. The reaction was quenched with ice water and diluted in dichloromethane. It was washed three times with water, dried using $MgSO_4$ and the solvent was evaporated by a rotary evaporator. The obtained solid was purified by column chromatography with an eluent of petroleum ether/ethyl acetate (5:1), and the solvent was evaporated by a rotary evaporator to obtain $FcOC_2SH$ (1.1 g, 4.2 mmol, 42% yield). ^{1}H NMR (399.7 MHz, Chloroform-d): δ = 4.8 (dt, J = 5.6, 2.0 Hz, 2H), 4.5 (dt, J = 6.2, 2.0 Hz, 2H), 4.2 (d, J = 4.9 Hz, 5H), 3.7 (s, 2H). ^{13}C NMR (100 MHz, Chloroform-d): δ = 198.69, 72.84, 70.04, 69.78, 38.26 ppm.

Synthesis of Ferrocene-hexan-6-one-1-thiol ($FcOC_6SH$)

$FcOC_6SH$ was synthesized following a previously described procedure.[71] This consisted in a Friedel−Crafts acylation to obtain

https://doi.org/10.1021/acsnano.5c13838
ACS Nano 2026, 20, 3487−3498

ferrocene-hexanone-1-bromide ($FcOC_6Br$) followed by a thiolation to obtain the final product. **Synthesis of $FcOC_6Br$.** A 50 mL round-bottom flask was charged with ferrocene (5.50 g, 35.2 mmol), DCM (15 mL) and $AlCl_3$ (2.19 g, 14.0 mmol) and put under argon at 0 °C under stirring. 6-bromohexanoyl chloride (1.96 mL,12.7 mmol) dissolved in DCM (5 mL) was added dropwise. After 2 h the reaction was quenched with water, diluted with DCM, and washed twice with water. The organic layer was dried over $MgSO_4$, and the solvent removed by rotary evaporation. The obtained solid was purified via column chromatography with hexane as eluent to elute unreacted Fc. Gradually, ethyl acetate was added to the eluent to obtain the product (2.76 g, 7.59 mmol, 60% yield). ^{1}H NMR (399.7 MHz, Chloroform-d): δ = 4.77 (t, J = 1.9 Hz, 2H), 4.48 (t, J = 1.9 Hz, 2H), 4.18 (s, 3H), 3.43 (t, J = 6.8 Hz, 2H), 2.71(t, J = 7.4 Hz, 2H), 1.90 (p, J = 14.9, 7.8, 7.4 Hz, 2H), 1.73 (p, 2H), 1.53 (m, 2H). ^{13}C NMR (100 MHz, Chloroform-d): δ = 204.3, 79.0, 72.2, 69.7, 69.3, 39.4, 33.7, 32.6, 28.0, 23.6 ppm. **Synthesis of $FcOC_6SH$.** A 25 mL round-bottom flask was charged with $FcOC_6Br$ (930 mg, 2.56 mmol), put under argon, added $(TMS)_2S$ (654 μL, 3.07 mmol) and THF (5 mL), and cooled to 0 °C under stirring. A TBAF solution (2.82 mL, 2.82 mmol, 1 M in THF) was added dropwise. After 70 min the reaction was quenched with ice water, diluted with diethyl ether and washed five times with water. The organic layer was dried over $MgSO_4$, and the solvent was removed by rotary evaporation. The obtained solid was purified by column chromatography with an eluent of hexane/ethyl acetate (4:1) to separate residual Fc and a dithiol impurity from the desired product. This resulted in $FcOC_6SH$ (406 mg, 1.28 mmol, 50% yield). ^{1}H NMR (399.7 MHz, Chloroform-d): δ = 4.78 (t, J = 1.7 Hz, 2H), 4.49 (t, J = 1.7 Hz, 2H), 4.19 (s, 5H), 2.71 (t, J = 7.3 Hz, 2H), 2.56 (q, J = 7.4 Hz, 2H), 1.71 (m, 2H), 1.49 (m, 1H), 1.36 (t, J = 7.8, 1.4 Hz, 1H). ^{13}C NMR (100 MHz, Chloroform-d): δ = 204.3, 79.1, 72.1, 69.7, 69.3, 39.4, 33.8, 28.2, 24.5, 23.9 ppm.

Anchoring Redox Ligands onto PbS QDs

Anchoring $FcOC_2SH$ or $FcOC_6SH$ onto PbS QDs was performed by mixing 500 μL of the obtained PbS solution with 500 μL of chloroform and 1 mL of a solution of $FcOC_2SH$ or $FcOC_6SH$ in chloroform at concentrations between 100 mM and 5 mM. This solution was left stirring overnight at room temperature in a glovebox. The ligand exchanged particles were purified by washing them with acetone (12 mL) and tetrachloroethylene (1 mL) three times to discard unreacted $FcOC_2SH$ or $FcOC_6SH$. The precipitate was dried under vacuum for 10 min and redissolved in tetrachloroethylene, except for the NMR measurements where the precipitate was redissolved in $CDCl_3$.

X-ray Photoelectron Spectroscopy

The XPS measurements were performed under UHV ($<2 \times 10^{-7}$ mbar) on a Thermo Fisher K-Alpha equipped with an Al Kα source. The XPS samples were prepared by drop casting 20 μL of the QD solution onto a cleaned ITO on glass substrate. The ITO substrate was cleaned by thoroughly rinsing it with acetone and isopropanol and put for 20 min in a UV/O_3 chamber.

Transmission Electron Microscopy

Transmission electron microscopy images were acquired using a JEOL JEM1400 transmission electron microscope operating at 120 keV. The TEM samples were prepared by drop casting a diluted QD solution onto the carbon-coated copper TEM grids. Size distributions were calculated using the software ImageJ from at least 100 QDs.

Nuclear Magnetic Resonance Spectroscopy

Solution ^{1}H and ^{13}C NMR spectra were collected with a 400 MHz Agilent spectrometer (^{1}H:399.7 MHz; ^{13}C 100 MHz). All samples were prepared in Chloroform-d3 and referenced to the residual protons or 13C nuclei in the NMR solvent relative to $(CH_3)_4Si$ (δ [ppm]); ^{1}H: Chloroform-d δ = 7.26 ppm.

Transient Absorption Spectroscopy

The QD samples were prepared by diluting them in tetrachloroethylene to obtain an absorbance of ca. 0.1 O.D. The measurement was performed in a 2 mm path length cuvette under vigorous stirring to avoid charging. Laser pulses of 180 fs were generated in a Yb:KGW oscillator (Light Conversion, Pharos SP) at 1028 nm and amplified. A small fraction of the 1028 nm fundamental beam was split off to generate the broadband probe spectrum in a sapphire crystal. The probe pulse was delayed up to 3 ns using an automated delay stage. Most of the 1028 nm fundamental beam was used as a pump pulse after nonlinear frequency mixing in an OPA and second harmonics module (Light Conversion, Orpheus) to achieve wavelengths of 310–1500 nm. The pump and probe pulses overlap on the sample position under an angle of ~8°, after which the pump pulse is dumped and the probe light is led to a detector suitable for the probe spectrum selected (Ultrafast Systems, Helios). All shown data is corrected for dispersion by fitting a polynomial function to the solvent response.

Absorption Spectroscopy

Steady-state absorption spectra of PbS QDs were recorded using a PerkinElmer Lambda 1050 UV/vis/NIR spectrophotometer.

Photoluminescence Spectroscopy

The QD samples were prepared by diluting them in tetrachloroethylene to obtain an absorbance of ca. 0.1 O.D. An Edinburgh Instruments FLS980 spectrofluorometer with double grating monochromators for both excitation and emission paths and a 450 W xenon lamp as an excitation source were used. The PLQY was measured using an Edinburgh Instruments FLS980 spectrometer with a calibrated integrating sphere. The emission was recorded between 650 to 1700 nm, and the samples were excited at 700 nm.

Time-Resolved Photoluminescence

The QD samples were prepared by diluting them in tetrachloroethylene to obtain an absorbance of ca. 0.1 O.D. An Edinburgh Instruments LifeSpec TCSPC with a 700 nm pulsed laser was used for recording the PL decay traces at the PL emission peak.

■ ASSOCIATED CONTENT

Data Availability Statement

The data supporting the findings of this study are provided in the paper and/or the Supporting Information. The data necessary to interpret, verify, and extend the research generated in this study have been deposited in 4TU.ResearchData.

Supporting Information

The Supporting Information is available free of charge at https://pubs.acs.org/doi/10.1021/acsnano.5c13838.

Materials and Methods: Theoretical considerations to develop the experimental model; derivation of the free energy of charge separation and recombination; PbS synthesis and characterization; PbS-$FcOC_2SH$ characterization; average number of excitons per QD, charge carrier dynamics of PbS and PbS-$FcOC_2SH$; charge carrier dynamics of PbS and PbS-$FcOC_2SH$, determination of the free energy of charge separation and charge recombination; kinetic model for PbS and PbS-$FcOC_2SH$; determination of PL, radiative, and nonradiative rates; comparison of PLQY with TA data of PbS; influence of linker length on charge transfer; rate constants of CS and CR as a function of bandgap; rate constants of CS and CR as a function of temperature (PDF)

■ AUTHOR INFORMATION

Corresponding Author

Yan B. Vogel − *Department of Chemical Engineering, Delft University of Technology, Delft 2629 HZ, The Netherlands;*

https://doi.org/10.1021/acsnano.5c13838
ACS Nano 2026, 20, 3487−3498

orcid.org/0000-0003-1975-7292; Email: y.b.vogel@tudelft.nl

Authors

Willemijn Boeije − *Department of Chemical Engineering, Delft University of Technology, Delft 2629 HZ, The Netherlands*

Lotte van Steekelenburg − *Department of Chemical Engineering, Delft University of Technology, Delft 2629 HZ, The Netherlands*

Demi Vollebregt − *Department of Chemical Engineering, Delft University of Technology, Delft 2629 HZ, The Netherlands*

Reinout Ubbink − *Department of Chemical Engineering, Delft University of Technology, Delft 2629 HZ, The Netherlands*

Hua Chen − *Department of Chemical Engineering, Delft University of Technology, Delft 2629 HZ, The Netherlands;* orcid.org/0009-0002-3391-9403

Ali Tayefeh Younesi − *Max Planck Institute for Polymer Research, Mainz 55128, Germany*

Ronald Ulbricht − *Max Planck Institute for Polymer Research, Mainz 55128, Germany*

Wolter F. Jager − *Department of Chemical Engineering, Delft University of Technology, Delft 2629 HZ, The Netherlands*

Ferdinand Grozema − *Department of Chemical Engineering, Delft University of Technology, Delft 2629 HZ, The Netherlands*

Arjan J. Houtepen − *Department of Chemical Engineering, Delft University of Technology, Delft 2629 HZ, The Netherlands*

Complete contact information is available at: https://pubs.acs.org/10.1021/acsnano.5c13838

Author Contributions

#W.B. and L.V.S. contributed equally. Y.B.V. conceived and supervised the project and performed most of the experiments. W.B. performed part of the transient absorption spectroscopy experiments. L.V.S. performed part of the transient absorption spectroscopy experiments and developed the fitting model. D.V. developed the molecular synthesis. R.U. performed the X-ray photoelectron spectroscopy experiments. H.C. performed the transmission electron microscopy experiments. A.T.Y. and R.U. contributed to the interpretation of the results. W.J. supervised the molecular synthesis. F.G. contributed to the interpretation of the results and the development of the fitting model. A.H. supervised the project and contributed to the interpretation of the results. All the authors contributed to the writing of the article and the interpretation of the results.

Notes

A version of this manuscript was previously made available as a preprint on Research Square: Vogel, Yan; Boeije, Willemijn; van Steekelenburg, Lotte; Vollebregt, Demi; Ubbink, Reinout; Chen, Hua; Younesi, Ali; Ulbricht, Ronald; Jager, Wolter; Grozema, Ferdinand; Houtepen, Arjan. The mechanism of charge transfer between quantum dots and redox molecules. 2025. Research Square. 10.21203/rs.3.rs-5957346/v1 (accessed February 27, 2025).

The authors declare no competing financial interest.

■ ACKNOWLEDGMENTS

Y.B.V. acknowledges the support from the Swiss National Science Foundation Postdoc Mobility Fellowship (P500PN_214333). Y.B.V. acknowledges the support provided by Jos Thieme for the transient absorption spectroscopy measurements, Bahiya Ibrahim for general laboratory maintenance, and Stephen Eustace for support with the NMR measurements.

■ REFERENCES

(1) Kim, T.; Kim, K.-H.; Kim, S.; Choi, S.-M.; Jang, H.; Seo, H.-K.; Lee, H.; Chung, D.-Y.; Jang, E. Efficient and Stable Blue Quantum Dot Light-Emitting Diode. *Nature* **2020**, *586*, 385−389.

(2) Wang, Y.-K.; Wan, H.; Teale, S.; Grater, L.; Zhao, F.; Zhang, Z.; Duan, H.-W.; Imran, M.; Wang, S.-D.; Hoogland, S.; et al. Long-Range Order Enabled Stability in Quantum Dot Light-Emitting Diodes. *Nature* **2024**, *629*, 586−591.

(3) Kim, D. C.; Seung, H.; Yoo, J.; Kim, J.; Song, H. H.; Kim, J. S.; Kim, Y.; Lee, K.; Choi, C.; Jung, D.; et al. Intrinsically Stretchable Quantum Dot Light-Emitting Diodes. *Nat. Electron.* **2024**, *7*, 365−374.

(4) Xu, H.; Song, J.; Zhou, P.; Song, Y.; Xu, J.; Shen, H.; Fang, S.; Gao, Y.; Zuo, Z.; Pina, J. M.; et al. Dipole−Dipole-Interaction-Assisted Self-Assembly of Quantum Dots for Highly Efficient Light-Emitting Diodes. *Nat. Photonics* **2024**, *18*, 186−191.

(5) Clifford, J. P.; Konstantatos, G.; Johnston, K. W.; Hoogland, S.; Levina, L.; Sargent, E. H. F. Sensitive and Spectrally Tuneable Colloidal-Quantum-Dot Photodetectors. *Nat. Nanotechnol.* **2009**, *4*, 40−44.

(6) Ban, H. W.; Vafaie, M.; Levina, L.; Xia, P.; Imran, M.; Liu, Y.; Najarian, A. M.; Sargent, E. H. Resurfacing of Inas Colloidal Quantum Dots Equalizes Photodetector Performance across Synthetic Routes. *J. Am. Chem. Soc.* **2024**, *146*, 24935−24944.

(7) Vafaie, M.; Fan, J. Z.; Morteza Najarian, A.; Ouellette, O.; Sagar, L. K.; Bertens, K.; Sun, B.; García de Arquer, F. P.; Sargent, E. H. Colloidal Quantum Dot Photodetectors with 10-Ns Response Time and 80% Quantum Efficiency at 1,550 Nm. *Matter* **2021**, *4*, 1042−1053.

(8) Ahn, N.; Livache, C.; Pinchetti, V.; Jung, H.; Jin, H.; Hahm, D.; Park, Y.-S.; Klimov, V. I. Electrically Driven Amplified Spontaneous Emission from Colloidal Quantum Dots. *Nature* **2023**, *617*, 79−85.

(9) Park, Y.-S.; Roh, J.; Diroll, B. T.; Schaller, R. D.; Klimov, V. I. Colloidal Quantum Dot Lasers. *Nat. Rev. Mater.* **2021**, *6*, 382−401.

(10) Whitworth, G. L.; Dalmases, M.; Taghipour, N.; Konstantatos, G. Solution-Processed Pbs Quantum Dot Infrared Laser with Room-Temperature Tunable Emission in the Optical Telecommunications Window. *Nat. Photonics* **2021**, *15*, 738−742.

(11) Jiang, Y.; Weiss, E. A. Colloidal Quantum Dots as Photocatalysts for Triplet Excited State Reactions of Organic Molecules. *J. Am. Chem. Soc.* **2020**, *142*, 15219−15229.

(12) Liu, X.-Y.; Chen, H.; Wang, R.; Shang, Y.; Zhang, Q.; Li, W.; Zhang, G.; Su, J.; Dinh, C. T.; de Arquer, F. P. G.; et al. 0d−2d Quantum Dot: Metal Dichalcogenide Nanocomposite Photocatalyst Achieves Efficient Hydrogen Generation. *Adv. Mater.* **2017**, *29*, 1605646.

(13) Aqoma, H.; Lee, S.-H.; Imran, I. F.; Hwang, J.-H.; Lee, S.-H.; Jang, S.-Y. Alkyl Ammonium Iodide-Based Ligand Exchange Strategy for High-Efficiency Organic-Cation Perovskite Quantum Dot Solar Cells. *Nat. Energy* **2024**, *9*, 324−332.

(14) Sun, R.; Zang, J.; Lai, R.; Yang, W.; Ji, B. Near-Infrared-to-Visible Photon Upconversion with Efficiency Exceeding 21% Sensitized by Inas Quantum Dots. *J. Am. Chem. Soc.* **2024**, *146*, 17618−17623.

(15) Li, Q.; Wu, K.; Zhu, H.; Yang, Y.; He, S.; Lian, T. Charge Transfer from Quantum-Confined 0d, 1d, and 2d Nanocrystals. *Chem. Rev.* **2024**, *124*, 5695−5763.

(16) Zhu, H.; Yang, Y.; Wu, K.; Lian, T. Charge Transfer Dynamics from Photoexcited Semiconductor Quantum Dots. *Annu. Rev. Phys. Chem.* **2016**, *67*, 259−281.

(17) Olshansky, J. H.; Ding, T. X.; Lee, Y. V.; Leone, S. R.; Alivisatos, A. P. Hole Transfer from Photoexcited Quantum Dots:

The Relationship between Driving Force and Rate. *J. Am. Chem. Soc.* **2015**, *137*, 15567−15575.
(18) Zhu, H.; Yang, Y.; Hyeon-Deuk, K.; Califano, M.; Song, N.; Wang, Y.; Zhang, W.; Prezhdo, O. V.; Lian, T. Auger-Assisted Electron Transfer from Photoexcited Semiconductor Quantum Dots. *Nano Lett.* **2014**, *14*, 1263−1269.
(19) Wang, J.; Ding, T.; Gao, K.; Wang, L.; Zhou, P.; Wu, K. Marcus Inverted Region of Charge Transfer from Low-Dimensional Semiconductor Materials. *Nat. Commun.* **2021**, *12*, 6333.
(20) Olshansky, J. H.; Balan, A. D.; Ding, T. X.; Fu, X.; Lee, Y. V.; Alivisatos, A. P. Temperature-Dependent Hole Transfer from Photoexcited Quantum Dots to Molecular Species: Evidence for Trap-Mediated Transfer. *ACS Nano* **2017**, *11*, 8346−8355.
(21) Wei, Z.; Mulder, J. T.; Dubey, R. K.; Evers, W. H.; Jager, W. F.; Houtepen, A. J.; Grozema, F. C. Tuning the Driving Force for Charge Transfer in Perovskite−Chromophore Systems. *J. Phys. Chem. C* **2023**, *127*, 15406−15415.
(22) Cadena, D. M.; Sowa, J. K.; Cotton, D. E.; Wight, C. D.; Hoffman, C. L.; Wagner, H. R.; Boette, J. T.; Raulerson, E. K.; Iverson, B. L.; Rossky, P. J.; et al. Aggregation of Charge Acceptors on Nanocrystal Surfaces Alters Rates of Photoinduced Electron Transfer. *J. Am. Chem. Soc.* **2022**, *144*, 22676−22688.
(23) Lian, S.; Weinberg, D. J.; Harris, R. D.; Kodaimati, M. S.; Weiss, E. A. Subpicosecond Photoinduced Hole Transfer from a Cds Quantum Dot to a Molecular Acceptor Bound through an Exciton-Delocalizing Ligand. *ACS Nano* **2016**, *10*, 6372−6382.
(24) Knowles, K. E.; Malicki, M.; Weiss, E. A. Dual-Time Scale Photoinduced Electron Transfer from Pbs Quantum Dots to a Molecular Acceptor. *J. Am. Chem. Soc.* **2012**, *134*, 12470−12473.
(25) Fort, M. J.; Click, S. M.; Robinson, E. H.; He, F. M. C.; Bernhardt, P. V.; Rosenthal, S. J.; Macdonald, J. E. Minimizing the Reorganization Energy of Cobalt Redox Mediators Maximizes Charge Transfer Rates from Quantum Dots. *Angew. Chem., Int. Ed.* **2022**, *61*, No. e202202322.
(26) Yan, C.; Weinberg, D.; Jasrasaria, D.; Kolaczkowski, M. A.; Liu, Z.-J.; Philbin, J. P.; Balan, A. D.; Liu, Y.; Schwartzberg, A. M.; Rabani, E.; et al. Uncovering the Role of Hole Traps in Promoting Hole Transfer from Multiexcitonic Quantum Dots to Molecular Acceptors. *ACS Nano* **2021**, *15*, 2281−2291.
(27) Padgaonkar, S.; Eckdahl, C. T.; Sowa, J. K.; López-Arteaga, R.; Westmoreland, D. E.; Woods, E. F.; Irgen-Gioro, S.; Nagasing, B.; Seideman, T.; Hersam, M. C.; et al. Light-Triggered Switching of Quantum Dot Photoluminescence through Excited-State Electron Transfer to Surface-Bound Photochromic Molecules. *Nano Lett.* **2021**, *21*, 854−860.
(28) DuBose, J. T.; Kamat, P. V. Energy Versus Electron Transfer: Managing Excited-State Interactions in Perovskite Nanocrystal−Molecular Hybrids. *Chem. Rev.* **2022**, *122*, 12475−12494.
(29) Eagle, F. W.; Harvey, S.; Beck, R.; Li, X.; Gamelin, D. R.; Cossairt, B. M. Enhanced Charge Transfer from Coinage Metal Doped Inp Quantum Dots. *ACS Nanosci. Au* **2023**, *3*, 451−461.
(30) Schleusener, A.; Micheel, M.; Benndorf, S.; Rettenmayr, M.; Weigand, W.; Wächtler, M. Ultrafast Electron Transfer from Cdse Quantum Dots to an [Fefe]-Hydrogenase Mimic. *J. Phys. Chem. Lett.* **2021**, *12*, 4385−4391.
(31) Bertrand, P. Application of Electron Transfer Theories to Biological Systems. In *Long-Range Electron Transfer in Biology*; Springer, 2005; pp. 1−47.
(32) Miller, J. R.; Beitz, J. V.; Huddleston, R. K. Effect of Free Energy on Rates of Electron Transfer between Molecules. *J. Am. Chem. Soc.* **1984**, *106*, 5057−5068.
(33) Miller, J. R.; Calcaterra, L.; Closs, G. Intramolecular Long-Distance Electron Transfer in Radical Anions. The Effects of Free Energy and Solvent on the Reaction Rates. *J. Am. Chem. Soc.* **1984**, *106*, 3047−3049.
(34) Marcus, R. A. Electron Transfer Reactions in Chemistry: Theory and Experiment (Nobel Lecture). *Angew. Chem., Int. Ed.* **1993**, *32*, 1111−1121.
(35) Fox, L. S.; Kozik, M.; Winkler, J. R.; Gray, H. B. Gaussian Free-Energy Dependence of Electron-Transfer Rates in Iridium Complexes. *Science* **1990**, *247*, 1069−1071.
(36) Parada, G. A.; Goldsmith, Z. K.; Kolmar, S.; Pettersson Rimgard, B.; Mercado, B. Q.; Hammarström, L.; Hammes-Schiffer, S.; Mayer, J. M. Concerted Proton-Electron Transfer Reactions in the Marcus Inverted Region. *Science* **2019**, *364*, 471−475.
(37) Fajardo, A. M.; Lewis, N. S. Free-Energy Dependence of Electron-Transfer Rate Constants at Si/Liquid Interfaces. *J. Phys. Chem. B* **1997**, *101*, 11136−11151.
(38) Fajardo, A. M.; Lewis, N. S. Rate Constants for Charge Transfer across Semiconductor-Liquid Interfaces. *Science* **1996**, *274*, 969−972.
(39) Hamann, T. W.; Gstrein, F.; Brunschwig, B. S.; Lewis, N. S. Measurement of the Free-Energy Dependence of Interfacial Charge-Transfer Rate Constants Using Zno/H2o Semiconductor/Liquid Contacts. *J. Am. Chem. Soc.* **2005**, *127*, 7815−7824.
(40) Rehm, D.; Weller, A. Kinetics of Fluorescence Quenching by Electron and H-Atom Transfer. *Isr. J. Chem.* **1970**, *8*, 259−271.
(41) Koch, M.; Rosspeintner, A.; Adamczyk, K.; Lang, B.; Dreyer, J.; Nibbering, E. T. J.; Vauthey, E. Real-Time Observation of the Formation of Excited Radical Ions in Bimolecular Photoinduced Charge Separation: Absence of the Marcus Inverted Region Explained. *J. Am. Chem. Soc.* **2013**, *135*, 9843−9848.
(42) Gunner, M. R.; Dutton, P. L. Temperature and --.DELTA.G.degree. Dependence of the Electron Transfer from Bph. Cntdot.-to Qa in Reaction Center Protein from Rhodobacter Sphaeroides with Different Quinones as QA. *J. Am. Chem. Soc.* **1989**, *111* (9), 3400−3412.
(43) Chidsey, C. D. Free Energy and Temperature Dependence of Electron Transfer at the Metal-Electrolyte Interface. *Science* **1991**, *251*, 919−922.
(44) Chemmangat, A.; Chen, H.-T.; Kamat, P. V. Bandgap Engineering of Halide Perovskite Nanocrystals for Maximizing Hole Transfer: Accessing the Marcus Inverted Region. *J. Am. Chem. Soc.* **2025**, *147*, 25727−25737.
(45) Ushakova, E. V.; Litvin, A. P.; Parfenov, P. S.; Fedorov, A. V.; Artemyev, M.; Prudnikau, A. V.; Rukhlenko, I. D.; Baranov, A. V. Anomalous Size-Dependent Decay of Low-Energy Luminescence from Pbs Quantum Dots in Colloidal Solution. *ACS Nano* **2012**, *6*, 8913−8921.
(46) Kang, I.; Wise, F. W. Electronic Structure and Optical Properties of Pbs and Pbse Quantum Dots. *J. Opt. Soc. Am. B* **1997**, *14*, 1632−1646.
(47) Moreels, I.; Lambert, K.; Smeets, D.; De Muynck, D.; Nollet, T.; Martins, J. C.; Vanhaecke, F.; Vantomme, A.; Delerue, C.; Allan, G.; et al. Size-Dependent Optical Properties of Colloidal Pbs Quantum Dots. *ACS Nano* **2009**, *3*, 3023−3030.
(48) Scholz, F.; Dworak, L.; Matylitsky, V. V.; Wachtveitl, J. Ultrafast Electron Transfer from Photoexcited Cdse Quantum Dots to Methylviologen. *ChemPhysChem* **2011**, *12*, 2255−2259.
(49) Ding, T. X.; Olshansky, J. H.; Leone, S. R.; Alivisatos, A. P. Efficiency of Hole Transfer from Photoexcited Quantum Dots to Covalently Linked Molecular Species. *J. Am. Chem. Soc.* **2015**, *137*, 2021−2029.
(50) Wu, K.; Du, Y.; Tang, H.; Chen, Z.; Lian, T. Efficient Extraction of Trapped Holes from Colloidal Cds Nanorods. *J. Am. Chem. Soc.* **2015**, *137*, 10224−10230.
(51) Hines, M. A.; Scholes, G. D. Colloidal Pbs Nanocrystals with Size-Tunable near-Infrared Emission: Observation of Post-Synthesis Self-Narrowing of the Particle Size Distribution. *Adv. Mater.* **2003**, *15*, 1844−1849.
(52) Semonin, O. E.; Johnson, J. C.; Luther, J. M.; Midgett, A. G.; Nozik, A. J.; Beard, M. C. Absolute Photoluminescence Quantum Yields of Ir-26 Dye, Pbs, and Pbse Quantum Dots. *J. Phys. Chem. Lett.* **2010**, *1*, 2445−2450.
(53) Moreels, I.; Justo, Y.; De Geyter, B.; Haustraete, K.; Martins, J. C.; Hens, Z. S.-T. Bright, and Stable Pbs Quantum Dots: A Surface Chemistry Study. *ACS Nano* **2011**, *5*, 2004−2012.

https://doi.org/10.1021/acsnano.5c13838
ACS Nano 2026, 20, 3487−3498

(54) Vogel, Y. B.; Zhang, L.; Darwish, N.; Gonçales, V. R.; Le Brun, A.; Gooding, J. J.; Molina, A.; Wallace, G. G.; Coote, M. L.; Gonzalez, J.; et al. Reproducible Flaws Unveil Electrostatic Aspects of Semiconductor Electrochemistry. *Nat. Commun.* **2017**, *8* (1), 2066.
(55) Astruc, D. Why Is Ferrocene So Exceptional? *Eur. J. Inorg. Chem.* **2017**, *2017*, 6−29.
(56) Knauf, R. R.; Lennox, J. C.; Dempsey, J. L. Quantifying Ligand Exchange Reactions at Cdse Nanocrystal Surfaces. *Chem. Mater.* **2016**, *28*, 4762−4770.
(57) Hens, Z.; Martins, J. C. A Solution Nmr Toolbox for Characterizing the Surface Chemistry of Colloidal Nanocrystals. *Chem. Mater.* **2013**, *25*, 1211−1221.
(58) Berera, R.; van Grondelle, R.; Kennis, J. T. M. Ultrafast Transient Absorption Spectroscopy: Principles and Application to Photosynthetic Systems. *Photosynth. Res.* **2009**, *101*, 105−118.
(59) Vogel, Y. B.; Pham, L. N.; Stam, M.; Ubbink, R. F.; Coote, M. L.; Houtepen, A. J. Solvation Shifts the Band-Edge Position of Colloidal Quantum Dots by Nearly 1 Ev. *J. Am. Chem. Soc.* **2024**, *146*, 9928−9938.
(60) Spoor, F. C. M.; Kunneman, L. T.; Evers, W. H.; Renaud, N.; Grozema, F. C.; Houtepen, A. J.; Siebbeles, L. D. A. Hole Cooling Is Much Faster Than Electron Cooling in Pbse Quantum Dots. *ACS Nano* **2016**, *10*, 695−703.
(61) Sahami, S.; Weaver, M. J. Deficiencies of the Ferricinium-Ferrocene Redox Couple for Estimating Transfer Energies of Single Ions. *J. Solution Chem.* **1981**, *10*, 199−208.
(62) Brown, P. R.; Kim, D.; Lunt, R. R.; Zhao, N.; Bawendi, M. G.; Grossman, J. C.; Bulović, V. Energy Level Modification in Lead Sulfide Quantum Dot Thin Films through Ligand Exchange. *ACS Nano* **2014**, *8*, 5863−5872.
(63) Kodis, G.; Gould, I. R.; Matyushov, D. V. Violation of Fluctuation-Dissipation Relations for Electron Transfer in Nonpolar Solvents. *Phys. Rev. Res.* **2021**, *3*, 013109.
(64) Matyushov, D. V. Reorganization Energy of Electron Transfer. *Phys. Chem. Chem. Phys.* **2023**, *25*, 7589−7610.
(65) Yang, C.-H.; Wang, C.-I.; Wang, Y.-S.; Hsu, C.-P. Non-Negligible Outer-Shell Reorganization Energy for Charge Transfer in Nonpolar Systems. *J. Chem. Theory Comput.* **2024**, *20*, 6981−6991.
(66) Duncan, W. R.; Prezhdo, O. V. Temperature Independence of the Photoinduced Electron Injection in Dye-Sensitized Tio2 Rationalized by Ab Initio Time-Domain Density Functional Theory. *J. Am. Chem. Soc.* **2008**, *130*, 9756−9762.
(67) Zhang, B.; Liu, M.; Nie, C.; Wang, Z.; Zhang, H.; Du, J.; Zhu, J.; Wu, K. Temperature-Insensitive Electron Transfer in Quantum Dot−Molecule Hybrids Driven by Nuclear Quantum Tunneling. *Nano Lett.* **2025**, *25*, 11433−11439.
(68) Morris-Cohen, A. J.; Peterson, M. D.; Frederick, M. T.; Kamm, J. M.; Weiss, E. A. Evidence for a through-Space Pathway for Electron Transfer from Quantum Dots to Carboxylate-Functionalized Viologens. *J. Phys. Chem. Lett.* **2012**, *3*, 2840−2844.
(69) Bird, O. F.; Drbohlav, K. M.; Gowdy, E. K.; Flinkingshelt, F. A.; Pellows, L. M.; Hammel, B. F.; Layne, B. W.; Ardo, S.; Yang, J. Y.; Miller, K. A.; et al. Revealing the Influence of Binding Motifs on Electron Transfer and Recombination Kinetics for Cdse Quantum Dots Functionalized with a Modified Viologen. *J. Phys. Chem. C* **2025**, *129*, 5556−5570.
(70) Ferreira, A. P.; da Silva, J. L. F.; Duarte, M. T.; da Piedade, M. F. M.; Robalo, M. P.; Harjivan, S. G.; Marzano, C.; Gandin, V.; Marques, M. M. Synthesis and Characterization of New Organometallic Benzo[B]Thiophene Derivatives with Potential Antitumor Properties. *Organometallics* **2009**, *28*, 5412−5423.
(71) Tindale, J. J.; Hartlen, K. D.; Alizadeh, A.; Workentin, M. S.; Ragogna, P. J. Maleimide-Modified Phosphonium Ionic Liquids: A Template Towards (Multi)Task-Specific Ionic Liquids. *Chem. - Eur. J.* **2010**, *16*, 9068−9075.

https://doi.org/10.1021/acsnano.5c13838
ACS Nano 2026, 20, 3487−3498